MRI compatible electromagnetic actuator: magneto-thermal design and optimization

Boussad Moualek, Simon Chauviere, Lamia Belguerras, Smail Mezani, Thierry Lubin

MRI compatible electromagnetic actuator: magneto-thermal design and optimization

Boussad MOUALEK[1], Simon CHAUVIERE[1], Lamia BELGUERRAS[1], Smail MEZANI[1], Thierry LUBIN[1]
[1]*GREEN, Université de Lorraine, F-54000,* Nancy, France
boussad.moualek@univ-lorraine.fr

Abstract

Purpose - Development of an MRI safe iron free electrical actuator for MR guided surgical interventions.

Design/Methodology/Approach - The paper deals with the design of an MRI compatible electrical actuator. Three dimensional electromagnetic and thermal analytical models have been developed to design the actuator. These models have been validated through 3D finite element computations. The analytical models have been inserted in an optimization procedure that uses genetic algorithms to find the optimal parameters of the actuator.

Finding - The analytical models are very fast and precise compared to the FE models. The computation time is 0.1 s for the electromagnetic analytical model and 3 min for the FE one. The optimized actuator does not perturb imaging sequence even if supplied with a current 10 times higher than its rated one. Indeed, the actuator's magnetic field generated in the imaging area doesn't exceed 1 ppm of the B0 field generated by the MRI scanner. The actuator can perform up to 25 biopsy cycles without any risk to the actuator or the patient since he maximum temperature rise of the actuator is about 20°C. The actuator is compact and lightweight compared to its pneumatic counterpart.

Originality/Value - Our MRI compatible actuator uses the B_0 field generated by scanner as inductor. The design procedure uses magneto-thermal coupled models that can be adapted to the design of a variety actuation systems working in MRI environment.

Keywords - Iron-free actuator, MRI compatibility, Analytical model, Finite elements, LPTM

1 Introduction

Magnetic Resonance Imaging (MRI) is a non-invasive medical imaging technique that provides high-quality images. It is particularly useful for surgical interventions with real-time imaging feedback. The benefits of this technique are widely recognized by researchers for robot-guided surgical interventions [1].

Robotic systems compatible with MRI have been developed, including ultrasonic and pneumatic actuators [2], [3], [4] which have drawbacks such as image quality reduction or complicated systems.

Electrostatic actuation is an alternative that does not affect image quality but has low torque density [5].

There is curiously limited research on MRI-compatible electromagnetic actuators. In [6], the authors have proposed actuator topology powered and controlled by the MRI scanner gradient fields for needle guidance. This actuator uses ferrous spheres to convert electromagnetic energy into mechanical energy. However, force control is limited by the performance of the clinical scanner and this system generates artifacts on the MRI image. Note that artifacts can be reduced by modifying the type of imaging sequence, such as the Turbo Spin Echo sequence [7], [8]. In [9], the authors propose a dc current actuator. Such machine has the drawback of using a brushed commutator which has MRI compatibility issues and may also generate sparks.

The proposed research aims to develop a compact and flexible electromagnetic actuation device for robot-assisted surgical interventions guided by MRI. We propose the design of a synchronous iron-free electromagnetic actuator capable of operating in an MRI environment. The originality of the proposed actuator lies in the fact that it only consists of one armature while a standard electric machine has two (a dc field winding and an armature winding). In our case, the field winding corresponds to the B_0 magnetic field of the MRI scanner which results in a very compact actuation solution.

2 Actuator topology and analytical modeling

Figure 1 shows a 3D sketch of the complete system, including the actuator, the mechanical transmission, and the needle used for biopsies during MRI-guided surgeries.

Figure 2 shows a 3D view and 2D cross-section of the actuator which is placed in the constant field B_0 produced by the MRI scanner. This field being fixed, the actuator is therefore rotating, which requires slip rings to ensure the electrical supply of the three-phase winding. The nature of the B_0 field leads to a 2-pole motor. A basic 1 slot/pole/phase, 3-phase winding is considered which requires 6 slots to accommodate the winding. Rectangular coils disposed as shown in Figure 2 are considered in order to reduce the total length of the actuator.

2.1 Electromagnetic model

A 3D model is developed to compute the magnetic field generated by the actuator. Figure 3 shows a single rectangular coil of the 3-phase winding for which we computed the magnetic field distribution using the Biot-Savart law. We assume a line current rather than a volumetric current density. The current i in each linear segment of the rectangular coil corresponds to the total ampere-turns in each slot. Hence, this model is precise as far as the computation is performed on points far from the coil. This choice is made because it leads to fast analytical computations (necessary for optimization purposes) but also because the model is mainly used to check for MRI compatibility of the actuator. Indeed, we only need to compute the magnetic field in an imaging zone far from the actuator.

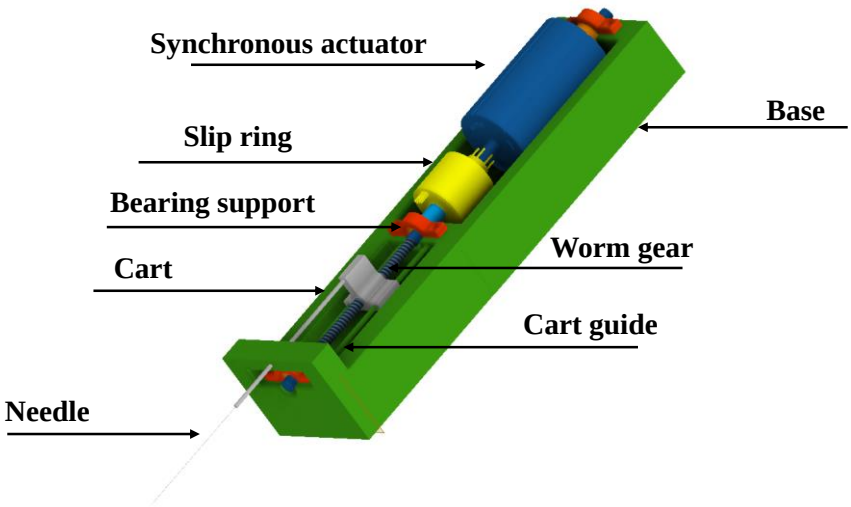

Fig. 1. Synchronous actuator with mechanical transmission and biopsy needle *(Source: Authors' own creation/work)*

The Biot-Savart law allows the computation of the flux density on point $M(r_M, \gamma, y_M)$ produced by a small current element located at point $N(r_N, \theta_N, y_N)$ on the coil's segment The coordinates(r_M, γ, y_M) correspond to the distance of point M from the y-axis, its angle to the vertical x-axis and its position along the y-axis, respectively. The same definition holds for the coordinates(r_N, θ_N, y_N) of point N. This field is integrated over the entire length of the conductor to get the final value of the flux density. In practice, the calculation is performed on the four linear segments of the coil. Segments 1 and 2 (parallel to the axis of rotation y) constitute the active part of the coil while segments 3 and 4 correspond to the end-windings.

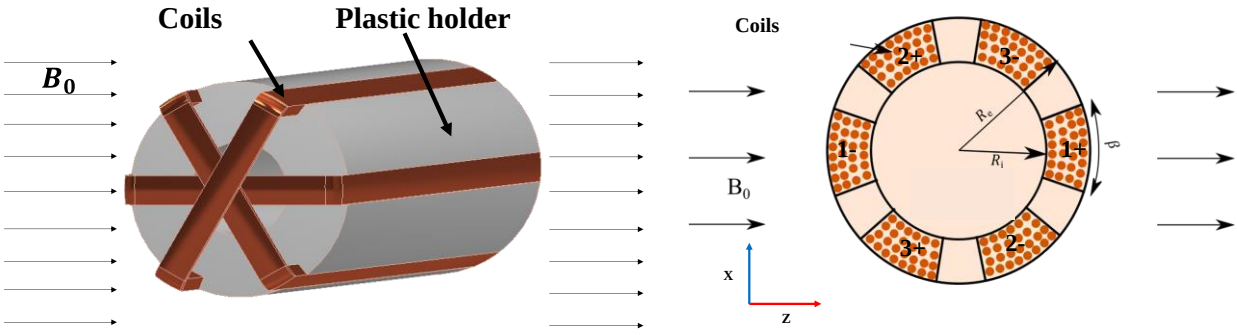

Fig. 2. 3D schematic of a 3-phase actuator in the constant MRI field B0 and 2D cross-section of actuator *(Source: Authors' own creation/work)*

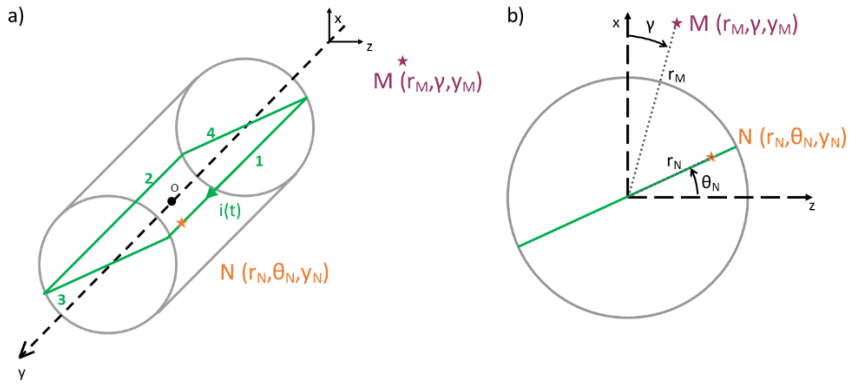

Fig. 3. Geometry of the 3D model with localized currents *(Source: Authors' own creation/work)*

The flux density created at point M by segment 1 (noted N_1) is given by:

$$\overrightarrow{B_1} = \int_{-L/2}^{L/2} \frac{\mu_0}{4\pi} \frac{i d\vec{l_1} \wedge (\overrightarrow{OM} - \overrightarrow{ON_1})}{\left|\overrightarrow{OM} - \overrightarrow{ON_1}\right|^3} \tag{1}$$

Points M and N_1 are located using two different cylindrical coordinate systems. The different vectors will be expressed in the Cartesian reference frame (u ⃗_x, u ⃗_y, u ⃗_z). We then have:

$$\begin{cases} d\vec{l_1} = dy_N \vec{u}_y \\ \overrightarrow{OM} = \begin{pmatrix} r_M \cos\gamma \\ y_M \\ r_M \sin\gamma \end{pmatrix} \\ \overrightarrow{ON_1} = \begin{pmatrix} R\sin\theta_N \\ y_N \\ R\cos\theta_N \end{pmatrix} \end{cases} \tag{2}$$

After integration of (1), the flux density expression becomes:

$$\overrightarrow{B_1} = \overrightarrow{U_1}\left[\frac{V\,(1+V^2/W_1)}{(V^2+W_1)^{\frac{3}{2}}} + \frac{V'(1+V'^2/W_1)}{(V'^2+W_1)^{\frac{3}{2}}}\right] \tag{3}$$

Where:

$$\begin{cases} \vec{U}_1 = \dfrac{\mu_0 i}{4\pi}\begin{pmatrix} r_M\sin\gamma - R\cos\theta_N \\ 0 \\ -r_M\cos\gamma + R\sin\theta_N \end{pmatrix} \\ \mathrm{V} = \dfrac{\mathrm{L}}{2} - y_M \quad , \qquad \mathrm{V}' = \dfrac{\mathrm{L}}{2} + y_M \\ \mathrm{W}_1 = r_M^2 + R^2 - 2r_M R\,\sin(\theta_N + \gamma) \end{cases} \tag{4}$$

The $\overrightarrow{B_2}$ field, corresponding to segment 2 in Figure 3, is calculated in the same way.

To find the field $\overrightarrow{B_3}$ created by segment 3, the vector $\overrightarrow{ON_3}$ is given by:

$$\overrightarrow{ON_3} = \begin{pmatrix} r_N\sin\theta_N \\ L/2 \\ r_N\cos\theta_N \end{pmatrix} \tag{5}$$

After integration of $\overrightarrow{dB_3}$ between $-R$ and R, we obtain:

$$\overrightarrow{B_3} = \overrightarrow{U_3}\left[\frac{R-X}{(Y_3-X^2)\sqrt{R^2-2RX+Y_3}} + \frac{R+X}{(Y_3-X^2)\sqrt{R^2+2RX+Y_3}}\right] \quad (6)$$

Where:

$$\begin{cases} \vec{U}_3 = \dfrac{\mu_0 i}{4\pi}\begin{pmatrix} \left(y_M - \frac{L}{2}\right)\cos\theta_N \\ -\mathrm{r_M}\cos(\theta_N+\gamma) \\ -\left(y_M-\frac{L}{2}\right)sin\theta_N \end{pmatrix} \\ \mathrm{X} = \mathrm{r_M}\sin(\theta_N+\gamma) \\ \mathrm{Y_3} = r_M^2 + \left(y_M-\frac{L}{2}\right)^2 \end{cases} \quad (7)$$

The same method as for $\overrightarrow{B_3}$ is used to calculate $\overrightarrow{B_4}$, corresponding to segment 4 in Figure 3.

The resulting field created by a phase coil at point M is the sum of the fields created by the four segments:

$$\vec{B}(M) = \vec{B}_1(M) + \vec{B}_2(M) + \vec{B}_3(M) + \vec{B}_4(M) \quad (8)$$

We then compute the fields created by each of the three phases by taking the following θ_N and i values:

$$\begin{cases} \theta_N = \theta \quad , & i = i_a = \sqrt{2}I\cos\theta \\ \theta_N = \theta - \dfrac{2\pi}{3} \quad , & i = i_b = \sqrt{2}I\cos\left(\theta - \dfrac{2\pi}{3}\right) \\ \theta_N = \theta + \dfrac{2\pi}{3} \quad , & i = i_c = \sqrt{2}I\cos\left(\theta + \dfrac{2\pi}{3}\right) \end{cases} \quad (9)$$

The total field is the sum of these three fields.

The value of ampere-turns I corresponds to the product of the slot's rms current density by the slot cross section area.

Regarding the torque produced by the actuator, a simple way to calculate its value is to use the Laplace force exerted on the winding. This force corresponds to the magnetic part of the Lorentz force which allows the determination of a local force density $\overrightarrow{f_m}$ (in N/m^3) on a point of a conductor carrying a current density $\vec{J}$ (in A/m²) by [10]:

$$\overrightarrow{f_m} = \vec{J} \times \vec{B} \quad (10)$$

Hence, the magnetic force exerted on an element volume dV of the conductor can be written as:

$$\overrightarrow{dF_m} = \overrightarrow{f_m}dV = (\vec{J} \times \vec{B})dV \quad (11)$$

The global force can then be calculated by integrating this element force over the entire conductor volume.

If the conductor is rotating around an axis of rotation, the element torque around a point O on this axis, calculated on a point M (resulting in a lever arm is $\overrightarrow{OM}$) is:

$$\overrightarrow{dC_m} = \overrightarrow{OM} \times (\vec{J} \times \vec{B})dV \quad (12)$$

The torque is then calculated by integrating this element torque over the entire conductor volume.

In the case of our actuator which is rotating around the y axis and by defining polar coordinates linked to the (xz) plane, we have:

$\vec{J} = J_m\overrightarrow{u_y}$, $\vec{B} = B_0\cos(\theta)\,\overrightarrow{u_r} + B_0\sin(\theta)\overrightarrow{u_\theta}$ and $\overrightarrow{OM} = r\overrightarrow{u_r}$

The torque is then calculated by integrating over the 3 coils of the actuator which results in the following relation:

$$C = 2\sqrt{2}\,J_s B_0\,L\,(R_e^3 - R_i^3)\sin(\beta/2) \quad (13)$$

Where J_s represents the rms value of the sinusoidal current density imposed in the slot, L is the active length of the actuator, R_e is the outer radius of the actuator, Ri is the inner radius of the actuator, and β is the angular opening of the slot.

Among the MRI compatibility criteria, the B_Z flux density produced by the actuator must not disturb the homogeneity of B_0 in order to ensure a good image quality free of artifacts [11]. In modern MRI scanners, the homogeneity of B_0 is about 1 ppm. Thus, an additional constraint imposes that the variation of the field due to the actuator, calculated at a certain radius R_0 around the rotation axis and an axial distance Y_{m0} away from the center of the actuator, does not exceed 1 ppm of B_0 (14)

$$B_Z \leq 10^{-6} B_0 \qquad (14)$$

The B_Z value is computed by the electromagnetic model.

2.2 Thermal model

A lumped parameter thermal model (LPTM) is developed to evaluate the actuator heating [12]. To build this model, each component of the actuator is represented by an elementary block that contains multiple independent unidirectional thermal circuits. Figure 4 shows the unidirectional thermal circuit of a parallelepipedal block in cartesian coordinates with a thermal conductivity k_y (along Oy axis), a power source P and a thermal capacitance C associated to the block. The lumped model consists of three thermal resistances, which allows the calculation of the average temperature. For radial heat flow, a similar circuit can be built [12]. In the multidimensional case, the model is constructed by linking each unidirectional lumped circuit to the average temperature node of the elementary blocks.

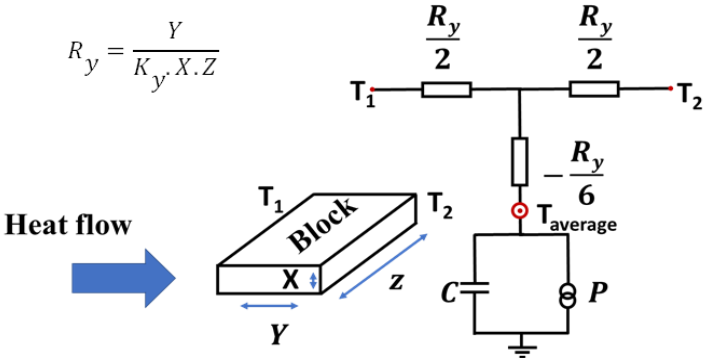

Fig. 4. Elementary block and its equivalent 1D thermal circuit. *(Source: Authors' own creation/work)*

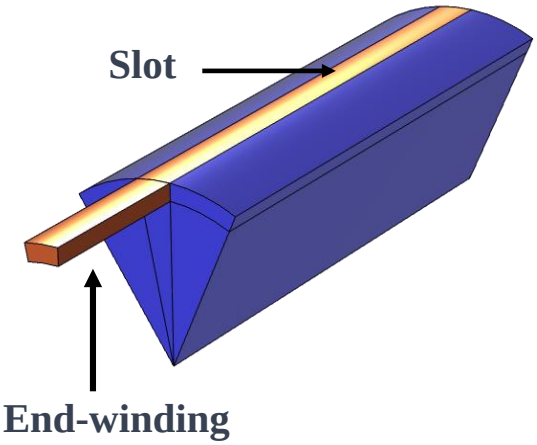

Fig. 5. 3D view of a tooth pitch of the actuator. *(Source: Authors' own creation/work)*

In the development of the LPTM, we consider a periodic slot pitch modeled in 3D. The end-winding is represented by a bar. The values of the thermal resistances and heat sources are calculated using the dimensions and losses issued from the electromagnetic model.

We consider the end winding as a parallelepiped-shaped bar (Figure 5), the length of which is equal to the actuator's diameter.

In the electromagnetic model, only joule losses exist in the winding in which a current density Js is imposed on the cross-section area of each coil. Hence, the Joule losses are computed

$$P = \rho_c J_s^2 \frac{V}{K_f} \qquad (15)$$

Where ρ_c represents the resistivity of copper, V denotes the volume of the coil, and K_f is the copper fill factor.
Note that we have separated the Joule losses in the active length and the end-winding in order to specify the right heat source in the thermal model in which the coil model uses separate thermal circuit for the end-winding and the active part.

It is worth noting that a convective thermal resistance is defined between the external surface of the actuator and the surrounding environment. For our actuator, which will operate at low speed, we use a convection coefficient h=5 W/(m². K).

Regarding the thermal conductivity (k) of different materials, we used standard values. The thermal conductivity of the isotropic plastic holder (k_p) is 0.17. The winding is made from insulated copper wires so the heat path in the orthogonal direction (x and z) sees successively copper and insulation in series. Hence, the equivalent conductivity mainly depends on the insulation thickness which result in low conductivity value of the coil in the orthogonal direction. It can be estimated according to the volume of insulation in the coil (set to 30% in our case). A value k_{cr}=0.17 W/(m·K) is considered according to literature [12]. In the axial direction, the thermal conductivity is close to that of copper (k_{ca}) whose value is 380 W/(m·K).

It is important to note that our model considers the transient regime. Therefore, to calculate the temperature rise of each node of the thermal model, we need to solve a system of ODEs (16).

$$\{p\} = [G\,]\{T\} + [C]\frac{d\{T\}}{dt} \qquad (16)$$

Where $\{p\}$ is the vector of losses issued from the electromagnetic model, $[G\,]$ is the conductance matrix, $[C]$ is the diagonal matrix of thermal capacitances and $\{T\}$ is the vector of node's temperature rise.

The thermal capacitance (C) in each domain is calculated by (17).

$$C = \rho\, Cp\, V \qquad (17)$$

Where ρ is the material's volumetric mass density, V is the volume of the domain, and C_p is the specific heat. For copper, we consider ($\rho = 8960\ kg/m^3$, $Cp = 380\ J/kgK$) and for plastic ($\rho = 1070\ kg/m^3$, $Cp = 1800\ J/kgK$).

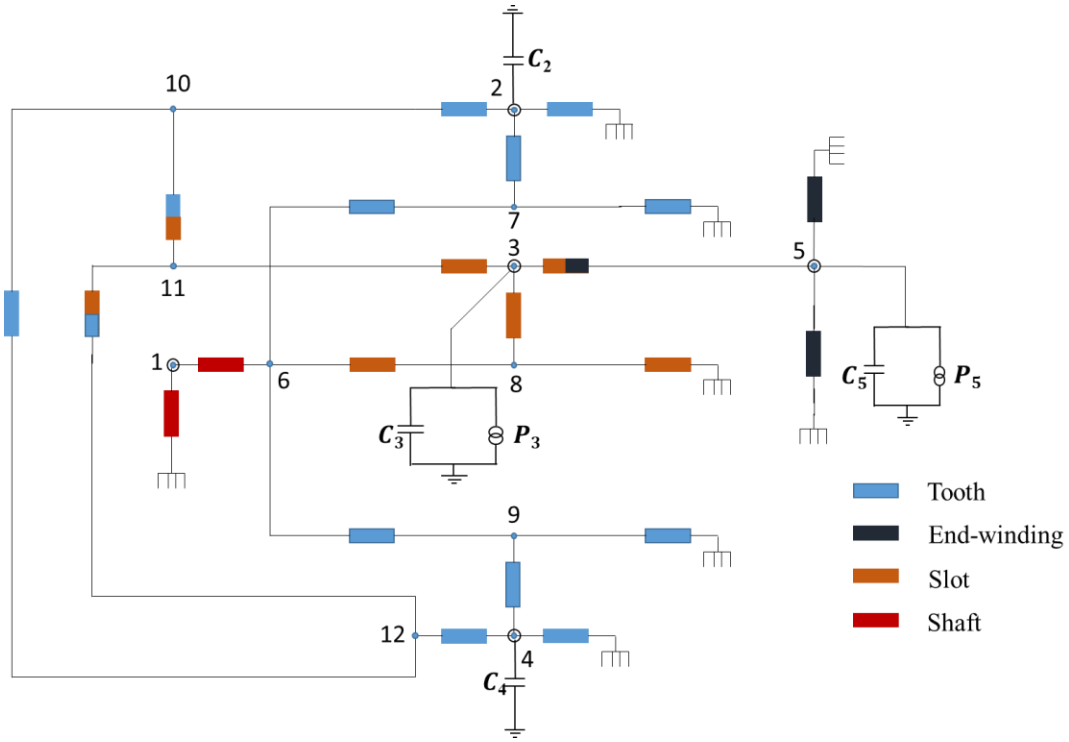

Fig. 6. LPTM model for our actuator. *(Source: Authors' own creation/work)*

Figure 6 illustrates the resulting LPTM model for our actuator, where each color corresponds to a specific part of the machine. The nodes represent locations of average temperature, identified by the numbers:

1) (Shaft)
2) (Tooth)
3) (Slot)

4) (Tooth)

5) (End-winding)).

It is noteworthy that thermal losses occur exclusively in the slot (node 3) and the end-winding (node 5). The thermal capacitances Ci are linked and injected into nodes numbered from 1 to 5.

3 Results

An actuator providing a torque of 50 mNm for B_0=3 T needed to obtain a force of 10N at the tip of the needle using the worm screw. The actuator was sized using the electromagnetic model while the transient thermal model checks the temperature rise of the different parts. The MRI compatibility constraint of 1 ppm is satisfied for R_0=40 mm and Y_{m0}=10 cm. As shown in figure 7, this corresponds to the area where we wish to perform the biopsy.

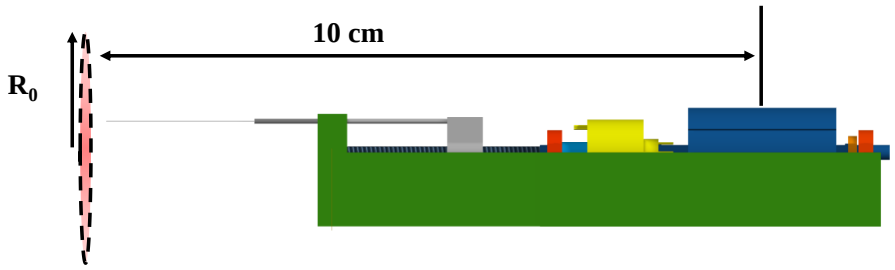

Fig. 7. Area where we would like to perform the biopsy. *(Source: Authors' own creation/work)*

Single objective constrained optimization using Matlab's Genetic Algorithm (GA) is used. The objective function is the minimization of the actuator's active volume. The variation range of the optimization parameters are listed in Table 1. The optimization was performed for a population of 800 and 200 maximum generations.

The optimization took 10 mn and stopped at generation n°10. It resulted in the following dimensions: active length of the actuator L= 30 mm, R_i =7 mm, R_e =8.1 mm, β =12 and J_s = 1 A/mm².

To validate the electromagnetic analytical calculations, a 3D Finite Element (FE) model was also established. Since the problem being addressed is an open-boundary one, the FE model external boundary was set far enough to enforce a zero-vector potential (typically $10R_e$). The mesh is dense to satisfactorily estimate the computed field in the imaging zone. However, this significantly increases the FE computation time compared to that of the analytical model (0.1 s vs. 3 mn).

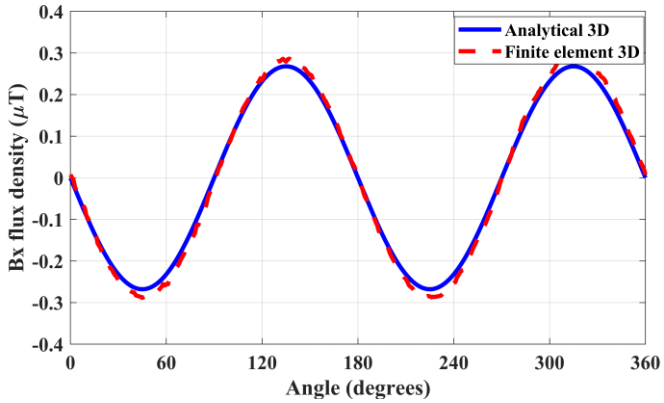

Fig. 8. OZ axis magnetic field calculated at R_0=40 mm and Y_{m0}=10 cm *(Source: Authors' own creation/work)*

Figure 8 illustrates the B_z flux density variation curve as a function of the angle. This plot is generated on a circle with a radius r=R_0=70 mm and Y_{m0}=10 cm for 10 times the rated current density (*10.J_s)*. The analytical and numerical calculations are in close agreement. Moreover, the peak-to-peak value calculated by FE is 0.6 µT, this value corresponds to a stress 5 times lower than the one stated in constraint (14).

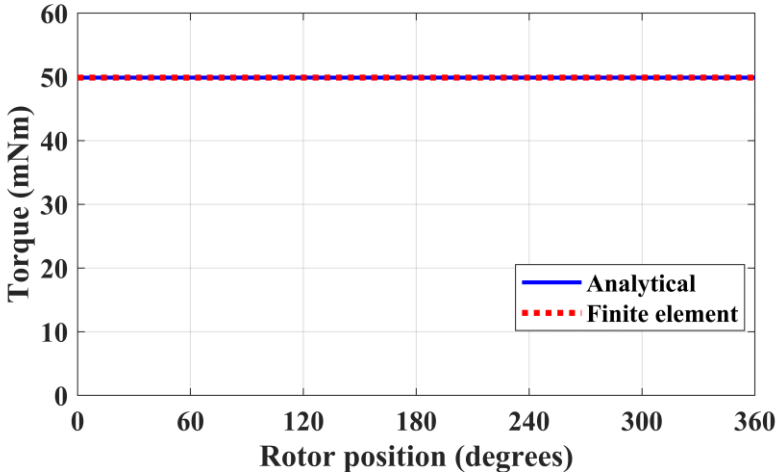

Fig. 9. Torque vs angular displacement of the actuator *(Source: Authors' own creation/work)*

The analytically and numerically calculated torques are close to 50 mNm, as shown in Figure 9. This corresponds to specifications for a current equivalent to 10 times the nominal current. As observed, there is no torque ripple. Indeed, torque ripples are typically caused by harmonics other than the fundamental. However, in this case, the B0 field generated by the MRI scanner remains constant and homogeneous, resulting in a perfectly sinusoidal electromotive force. The currents we apply are also purely sinusoidal, which results in a ripple-free torque.

To validate the equivalent thermal network, we also established a 3D Finite Element (FE) model. Figure 10 displays the temperature distribution (obtained using Comsol Multiphysics) of the optimized actuator for the rated current. The highest values are located in the coil heads, the hot spot reaches 2.6°C. The LPTM model provides a mean temperature-rise of about 2.5 °C. The cpu time of FE computation is 4 s while the LPTM is much faster (0.1 s).

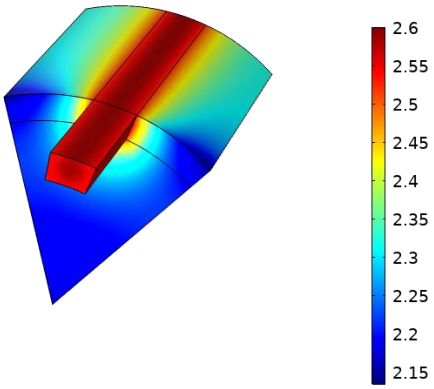

Fig. 10. Steady state temperature rise at rated current *(Source: Authors' own creation/work)*

During a sample extraction, the actuator drives a needle (using a lead screw/nut system not shown here) describing an operating cycle in which the rms current I in the actuator varies with time as follows:

a) Starting [0-1] s, $I=10I_0$: corresponds to a rapid transient put into motion of the needle to reach the rated speed (outside the skin)
b) Steady drive [1-7] s, $I=I_0$: corresponds to the phase where the skin is perforated
c) Locked in position |7-15] s, $I=5.I_0$: corresponds to the phase when the needle performs the biopsy sample
d) Reverse start [15-16] s, $I=10.I_0$: the needle is put into motion to go outside the skin
e) Reverse steady drive [16-22] s, $I=I_0$: the needle returns to its starting position described in a)
f) Idle state [22-40] s, $I=0$: the needle is in rest and ready for the next sampling cycle

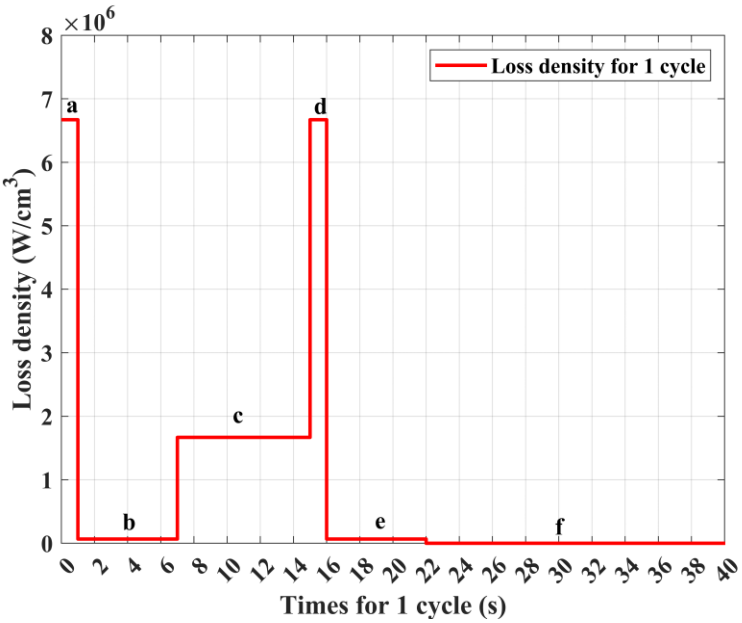

Fig. 11. Loss density evolution during one cycle of 6-steps biopsy sample *(Source: Authors' own creation/work)*

These operating steps corresponds to different current value so to different losses. The value of the loss densities, computed from the analytical electromagnetic model, are given in Figure 11 for each step. These values are used in the thermal model to calculate the heating of the actuator during the transient operation of the actuator.

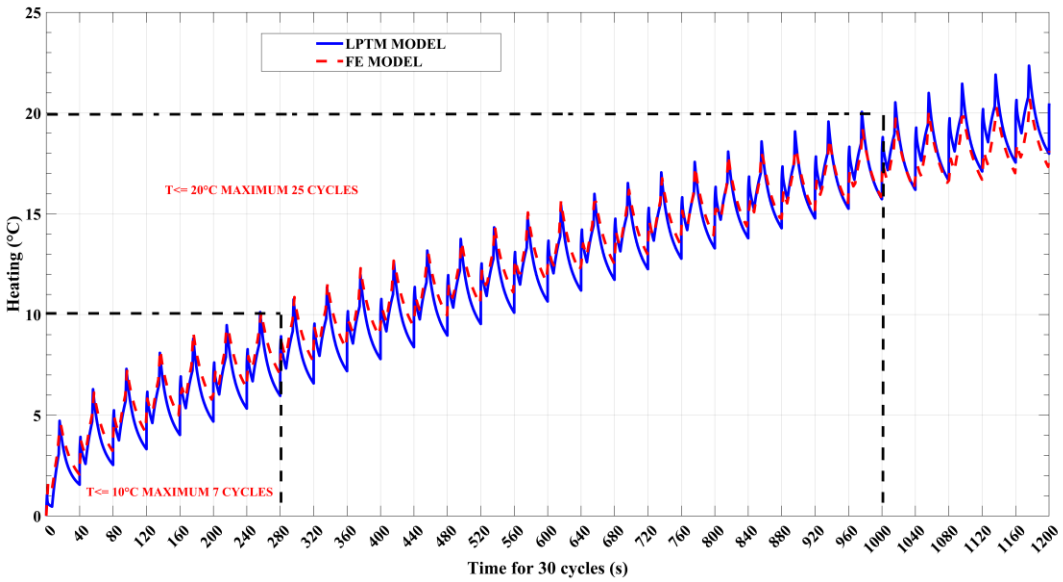

Fig. 12. Temperature-rise of the actuator during 30 operating cycles *(Source: Authors' own creation/work)*

Figure 12 shows the heating of the actuator during 30 cycles. It can be seen that the highest temperature-rise does not exceed 21.21 °C, making the operation safe in regard to the person's protection against any potential burn. It should be noted that the LPTM provides satisfactory results compared to the FE ones. If we want to limit the temperature rise of our actuator to 20°C, we can perform up to 25 consecutive cycles (Figure 11). For a more restrictive operation imposing a maximum temperature rise of 10°C, we can safely run 7 cycles.

4 Conclusion

We carried out a design and sizing study for an MRI-compatible electromagnetic actuator. Using electromagnetic and thermal modeling tools, we were able to determine the optimum dimensions to achieve the required torque, while respecting the constraints of homogeneity of the MRI B_0 field to avoid creating artifacts on the image. Thermal constraints were considered through 3D thermal calculations. We have determined optimal values for the dimensions of the actuator that will be used for prototyping. The preliminary test will be carried-out in a 0.3 T open portable MRI system realized in our Lab [13]. The modelling approach provides an initial basis for the design and optimization of electromagnetic actuators for biomedical applications, and can be extended to other application areas requiring high-performance actuators.

REFERENCES

[1] R. Gassert, A. Yamamoto, D. Chapuis, L. Dovat, H. Bleuler, et E. Burdet, « Actuation methods for applications in MR environments », Concepts Magn. Reson., vol. 29B, no 4, p. 191 209, oct. 2006, doi: 10.1002/cmr.b.20070.

[2] G. S. Fischer, A. Krieger, I. Iordachita, C. Csoma, L. L. Whitcomb, et G. Fichtinger, « MRI Compatibility of Robot Actuation Techniques – A Comparative Study », in Medical Image Computing and Computer-Assisted Intervention – MICCAI 2008, vol. 5242, D. Metaxas, L. Axel, G. Fichtinger, et G. Székely, Éd. Berlin, Heidelberg: Springer Berlin Heidelberg, 2008, p. 509 517. doi: 10.1007/978-3-540-85990-1_61.

[3] Hao Su, Gang Li, and Gregory S Fischer. Sensors, actuators, and robots for mri-guided surgery and interventions. Volume 3: Image-guided surgical procedures and interventions, pages 201–231, 2018.

[4] Vincent Groenhuis, Fran¸coise J Siepel, Jeroen Veltman, and Stefano Stramigioli. Design and characterization of stormram 4: An mri-compatible robotic system for breast biopsy. In 2017 IEEE/RSJ International Conference on Intelligent Robots and Systems (IROS), pages 928–933. IEEE, 2017.

[5] A. Yamamoto et al., « Evaluation of MR-compatibility of Electrostatic Linear Motor », in Proceedings of the 2005 IEEE International Conference on Robotics and Automation, Barcelona, Spain, 2005, p. 3658 3663. doi: 10.1109/ROBOT.2005.1570677.

[6] P. Vartholomeos, C. Bergeles, L. Qin, et P. E. Dupont, « An MRI-powered and controlled actuator technology for tetherless robotic interventions », The International Journal of Robotics Research, vol. 32, no 13, p. 1536 1552, nov. 2013, doi: 10.1177/0278364913500362.

[7] SP DiMaio, GS Fischer, SJ Haker, N Hata, I Iordachita, CM Tempany, R Kikinis, and G Fichtinger. A system for mri-guided prostate interventions. In the First IEEE/RAS-EMBS International Conference on Biomedical Robotics and Biomechatronics, 2006. BioRob 2006., pages 68–73. IEEE, 2006.

[8] Christos Bergeles, Panagiotis Vartholomeos, Lei Qin, and Pierre E Dupont. Closed-loop commutation control of an mri-powered robot actuator. In 2013 IEEE International Conference on Robotics and Automation, pages 698–703. IEEE, 2013.

[9] L. W. Hofstetter, J. R. Hadley, R. Merrill, H. Pham, G. C. Fine, et D. L. Parker, « MRI-compatible electromagnetic servomotor for image-guided medical robotics », *Communications Engineering*, vol. 1, nº 1, p. 4, mai 2022, doi: 10.1038/s44172-022-00001-y.

[10] S. R. H. Hoole, P. R. P. Hoole, *A Modern Short Course in Engineering Electromagnetics*. Oxford University Press, UK, 548 p., 1996.

[11] E. N. Manson, S. Inkoom, A. N. Mumuni, « Impact of Magnetic Field Inhomogeneity on the Quality of Magnetic Resonance Images and Compensation Techniques: A Review ». Reports in Medical Imaging. 2022; 15:43-5.

[12] P. H. Mellor, D. Roberts, and D. R. Turner, 1991, "Lumped parameter thermal model for electrical machines of TEFC design," IEE Proceedings-B, vol. 138, no. 5, pp. 205-218

[13] S. Chauviere, L. Belguerras, T. Lubin, et S. Mezani, « Design and test of an open portable MRI system », COMPEL - The international journal for computation and mathematics in electrical and electronic engineering, vol. 41, no 4, p. 1084 1095, janv. 2022, doi: 10.1108/COMPEL-11-2021-0436.